Radiation from a dipole embedded in a multilayer slab

S. R. J. Brueck,*,† V. A. Smagley,† and P. G. Eliseev

Center for High Technology Materials, University of New Mexico, Albuquerque, New Mexico 87106, USA

An analytical solution for the radiation emitted from a dipole embedded in an arbitrary, planar dielectric film stack is presented. The calculation uses a rigorous Hertz-vector formalism to treat the electromagnetic boundary conditions. The radiation fields are then evaluated in a far-field approximation to get the radiated fields far from the dipole. Both two-dimensional (2D) emission into bound modes of the dielectric stack and three-dimensional (3D) emission into radiation fields above and below the stack are evaluated. These solutions are explored for two simple cases: a InGaAs slab symmetrically clad with up to four high-contrast (Al_2O_3/GaAs) Bragg mirror pairs and semi-infinite air spaces, and a similar asymmetric structure with a GaAs substrate on one side. The symmetric structure supports both 2D bound and 3D radiation fields. The asymmetric structure only supports 3D radiation fields since there are no strictly bound modes, but "leaky" modes appear that are very similar to the bound modes in the symmetric structure except that the radiated power ultimately is transmitted into the substrate in a very highly directional beam. This calculation is applicable to a wide range of solid-state photonic devices, including vertical-cavity and edge-emitting lasers, spontaneous light-emitting diodes, and photodetectors.

PACS number(s): 41.20.−q, 42.25.−p, 42.55.−f, 42.82.−m

I. INTRODUCTION

The coupling of an electric dipole with electromagnetic fields in solids is fundamental to solid-state light emitting and detecting devices (LEDs, lasers, displays, photodetectors, etc.). In a uniform infinite medium the dipole radiation fields are very well known. The study of these radiation fields in the presence of metallic and dielectric interfaces has been a recurring topic in electromagnetism. Sommerfeld [1,2] made seminal contributions to the solution that provide the basis of the work presented here. He was concerned with issues of long-wavelength radio wave propagation over the surface of the earth and addressed the single interface problem of a dipole above a lossy dielectric. As is very well known [3,4], the addition of a second interface, e.g., a dipole embedded within a dielectric slab, adds significant complexity to the problem, since the radiation is now distributed between three-dimensional (3D) radiation out the sides of the slab and the two-dimensional (2D) bound modes supported by the slab. With the development of multilayer structures with very high, and precisely tailorable, reflectivities, such as vertical-cavity lasers, resonant cavity LEDs, and photodetectors, there is a need for a more detailed understanding of the distribution of the radiation between these components and the corresponding angular and thickness/wavelength dependencies. Both approximate analytic treatments [5,6] and numerical solutions [7] have appeared in the literature. Recently, two equivalent detailed analytical treatments for the simple slab case have been reported [4,8]. Both of these treatments presented fully analytic results for the radiation

into both the 2D bound modes and the 3D radiation modes and investigated in detail the dependence on dielectric contrast and slab thickness.

The purpose of this paper is to extend these results [4] to arbitrary multilayer dielectric structures and to investigate in particular the impact of high-reflectivity Bragg mirrors on the dipole radiation. The analysis is extended to asymmetric cases, including mode-free cases that support "leaky" modes that are not bound in the strict sense, but rather build up significant intensity within the multilayer structure and ultimately radiate their power into 3D radiation within the substrate.

Section II presents the Hertz vector formulation and introduces a significant algebraic simplification by introducing both electric and magnetic Hertz vectors. Section III presents the closed form analytic results for arbitrary multilayer structures. Detailed investigation of the results for a symmetric structure with high-reflectivity Bragg reflectors is presented in Sec. IV A. A related asymmetric structure with a high-index substrate is analyzed in Sec. IV B. Finally, conclusions are presented in Sec. V.

II. HERTZ VECTOR FORMULATION

A. Geometry of the problem

The geometry of the problem is shown in Fig. 1. A dipole is embedded in an arbitrary film stack taken as infinite in the (x,y) directions. The z direction is perpendicular to the films. The dipole is oriented at an angle θ_d from the z direction in the (x,z) plane. The layer stacks above and below the dipole have arbitrary numbers of layers with arbitrary relative dielectric constants ($\kappa_i = n_i^2$) and thicknesses (L_i). The total physical thicknesses of the top and bottom cladding layers from the position of the dipole to the edge of the outermost layer are L_{t-tot} and L_{b-tot}. For the sample calculations presented below, the inner cladding layers (shaded)

———————
*Also at Department of Electrical and Computer Engineering, University of New Mexico, Albuquerque, New Mexico 87131, USA. Email address: brueck@chtm.unm.edu

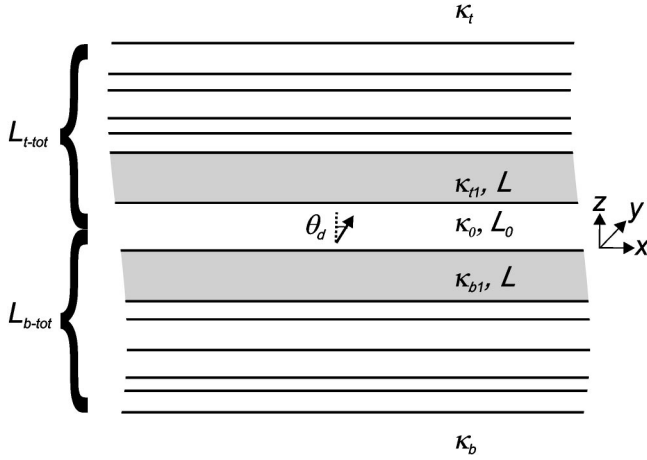†Also at Department of Physics and Astronomy, University of New Mexico, Albuquerque, New Mexico 87131, USA.

FIG. 1. Geometry of the problem. A radiating dipole oriented at an angle θ_d in the (x,z) plane is embedded in the center of a infinite slab of material of relative dielectric constant κ_0 and thickness L_0. The slab is bound with arbitrary film stacks ending in top and bottom semi-infinite media of relative dielectric constant κ_t and κ_b. For the example calculations, the shaded inner cladding thicknesses L are identical and variable. The total physical thicknesses of the upper and lower claddings from the position of the dipole to the edge of the semi-infinite media are indicated by $L_{t\text{-tot}}$ and $L_{b\text{-tot}}$.

have identical dielectric constants, $\kappa_{t1} = \kappa_{b1} = \kappa = n^2$, and an equal thickness, $L_{t1} = L_{b1} = L$ that is varied in the calculation. The thickness of the layer containing the dipole is denoted as L_0.

B. Hertz vector formalism

In our previous paper [4] we used the Hertz vector formalism introduced by Sommerfeld [1] to evaluate the radiation from a simple dielectric slab structure. Lukosz [9,10] has developed an alternate formulation of the Hertz vector source terms that has the significant advantage that the boundary conditions are uncoupled for the TE and TM radiation from a horizontal dipole. This dramatically simplifies the algebra of the calculation; the final results are identical. Lukosz's formulation is briefly described here and is followed in the evaluations of the radiated power.

Lukosz [9,10] has shown that the electromagnetic field for any orientation of the dipole can be represented by two scalar functions, $\phi(\vec{x})$ and $\psi(\vec{x})$, which are the z components (perpendicular to the layers) of an electric and a magnetic Hertz vector, respectively,

$$\vec{\Pi}^{(E)}(\vec{x}) = (0,0,\phi(\vec{x})),$$

$$\vec{\Pi}^{(H)}(\vec{x}) = (0,0,\psi(\vec{x})). \tag{1}$$

Both scalar functions satisfy the homogeneous Hemholtz equation in source-free regions, viz.,

$$(\nabla^2 - \kappa_i \varepsilon_0 k_0^2)\phi(\vec{x}) = (\nabla^2 - \kappa_i \varepsilon_0 k_0^2)\psi(\vec{x}) = 0, \tag{2}$$

where ε_0 is the free-space permittivity, $\kappa_i = n_i^2$ is the relative dielectric permittivity of the medium, and $k_0 = \omega/c$ is the magnitude of the free-space photon wave vector. The fields are given by

$$\vec{E}(\vec{x}) = i\omega\vec{\nabla} \times \vec{\Pi}^{(H)}(\vec{x}) + (\kappa\varepsilon_0)^{-1}\vec{\nabla} \times \vec{\nabla} \times \vec{\Pi}^{(E)}(\vec{x}),$$

$$\vec{H}(\vec{x}) = -i\omega\vec{\nabla} \times \vec{\Pi}^{(E)}(\vec{x}) + (\mu_0)^{-1}\vec{\nabla} \times \vec{\nabla} \times \vec{\Pi}^{(H)}(\vec{x}). \tag{3}$$

where ε_0 and μ_0 are the free-space values of the electric and magnetic permeabilities, respectively.

From Eqs. (1) and (3) it is straightforward to show that $\phi(\vec{x})$ corresponds to a TM wave and $\psi(\vec{x})$ describes a TE wave; since these are orthogonal there is no coupling between them. In the Sommerfeld basis [1], there is only an electric Hertz vector with components both in the z direction and in the x direction; the boundary conditions at interfaces are coupled which algebraically complicates the general solution for an arbitrary film stack.

C. Expansion of the dipole field into TE and TM plane waves

To begin the calculation, it is necessary to express the field of a dipole, located at the origin in an infinite medium, in a superposition of TE and TM plane waves. Then the boundary value problem for each independent plane wave can be directly solved by standard thin-film electromagnetic methods; finally the results are transformed back to real space using the techniques developed by Sommerfeld [1,2,11].

The infinite-medium real-space electric-Hertz vector corresponding to a dipole is simply

$$\vec{\pi}(\vec{x}) = p_o \frac{e^{in_i k_0 r}}{4\pi\varepsilon_0\kappa_i r}(\sin\theta_d\hat{e}_x + \cos\theta_d\hat{e}_z), \tag{4}$$

where p_o is the dipole moment, $(\hat{e}_x, \hat{e}_y)$ are unit vectors in the corresponding directions. The total radiated power for this dipole in an infinite medium is given by the well-known result [12]

$$P_{\text{inf}} = \frac{k_o^4 \text{Re}(n_i)|p_o|^2}{12\pi\eta_0\varepsilon_0^2}, \tag{5}$$

where $\eta_0 = \sqrt{\mu_0/\varepsilon_0}$. In the following, radiated powers are shown normalized to this value. The corresponding Fourier transform of the infinite-medium Hertz vector is

$$\vec{\Pi}_\infty^{(E)}(\vec{K}) = \frac{p_o}{\varepsilon_0\kappa_i k_0^2} \frac{1}{K^2 - \kappa_i}(\sin\theta_d\hat{e}_x + \cos\theta_d\hat{e}_z)$$

$$\equiv \Phi(K)(\sin\theta_d\hat{e}_x + \cos\theta_d\hat{e}_z), \tag{6}$$

where $k_0 K$ is the transform coordinate. This expression can be put in a more suitable form for the planar geometry of the problem by carrying out the inverse transform in the z direction and expressing the remaining integrals in cylindrical coordinates,

$$\Phi(\rho,z) = \frac{p_o}{\kappa_i}\int_0^\infty \frac{k_0}{\gamma_i}e^{-\gamma_i|\tilde{z}|}J_0(\lambda\tilde{\rho})\lambda d\lambda$$

$$= \frac{p_o}{2\kappa_i}\int_{-\infty}^\infty \frac{k_0}{\gamma_i}e^{-\gamma_i|\tilde{z}|}H_0^1(\lambda\tilde{\rho})\lambda d\lambda, \qquad (7)$$

where $k_0\lambda$ is the radial transform coordinate [$\lambda^2 = \xi^2 + \eta^2$ with $k_0\xi$ ($k_0\eta$) the $x(y)$-directed transform coordinate], $\tilde{\rho} = k_0\rho$ and $\tilde{z} = k_0z$ are the dimensionless radial and vertical spatial coordinates, and

$$\gamma_i = \sqrt{\lambda^2 - \kappa_i} \xrightarrow[\lambda\to 0]{} -in_i, \qquad (8)$$

where the sign of the square root is chosen to ensure $\mathrm{Re}(\gamma_i) > 0$ for convergence of Eq. (7). J_0 is the zeroth-order Bessel function and H_0^1 is the Hankel function of the first kind of zeroth order. The second form of this expression will be useful for evaluation of the complex integrations since the integration extends along the entire λ axis.

The scalars ϕ and ψ for the unbounded medium are found in terms of Φ by equality of the z components of the electric and magnetic fields from Eqs. (3) and (6), giving

$$\phi(\xi,\eta;z) = \Phi(\lambda;z)\left(\cos\theta_d \mp i\frac{\xi\gamma_i}{\lambda^2}\sin\theta_d\right) \qquad (9a)$$

and

$$\psi(\xi,\eta;z) = \Phi(\lambda;z)\left(\eta_0\frac{\eta}{\lambda^2}\sin\theta_d\right), \qquad (9b)$$

where the $(-)$ sign in Eq. (9a) is appropriate in the upper half plane ($z > 0$) and the $(+)$ sign in the lower half plane ($z < 0$). For a vertical dipole ($\sin\theta_d = 0$) there are only TM waves (*only a single* scalar function $\phi(\xi,\eta;z)$ is required); for a horizontal dipole ($\sin\theta_d = 1$) there are both TM and TE waves [*both* scalar functions $\phi(\xi,\eta;z)$ and $\psi(\xi,\eta;z)$ are required]. The source terms for a horizontal dipole ($\sin\theta_d = 1$) depend on the transverse transform coordinates (ξ,η) which results in a dependence of the radiated fields on the polar angle φ where $\varphi = 0$ is the radial direction parallel to the dipole.

III. EVALUATIONS OF THE RADIATED FIELDS AND POWER

A. Boundary value problem and evaluation of the Hertz potential; vertical dipole ($\cos\theta_d = 1$)

The boundary conditions for ϕ at an interface between media 1 and 2 are [9]

$$\phi_1 = \phi_2,$$

$$\frac{1}{\kappa_1}\frac{\partial\phi_1}{\partial z} = \frac{1}{\kappa_2}\frac{\partial\phi_2}{\partial z}. \qquad (10)$$

It is a standard multiple-interface thin-film matrix-analysis problem to solve for the Hertz potential everywhere. The result is

$$\phi_0^V = \frac{p_o}{2\kappa_1}\int_{-\infty}^\infty \frac{k_0}{\gamma_0}H_0^1(\lambda\tilde{\rho})\lambda d\lambda$$

$$\times\left[\frac{e^{-\gamma_0\tilde{L}_0}R_b^p(1+e^{-\gamma_0\tilde{L}_0}R_t^p)}{1-e^{-2\gamma_0\tilde{L}_0}R_b^pR_t^p}e^{-\gamma_0\tilde{z}}\right.$$

$$\left.+\frac{e^{-\gamma_0\tilde{L}_0}R_t^p(1+e^{-\gamma_0\tilde{L}_0}R_b^p)}{1-e^{-2\gamma_0\tilde{L}_0}R_b^pR_t^p}e^{\gamma_0\tilde{z}}+e^{-\gamma_0|\tilde{z}|}\right] \qquad (11)$$

for the slab region (subscript 0), and

$$\phi_t^V = \frac{p_o}{2\kappa_t}\int_{-\infty}^\infty \frac{k_0}{\gamma_t}H_0^1(\lambda\tilde{\rho})\lambda d\lambda$$

$$\times\left[\frac{T_t^pe^{-\gamma_0\tilde{L}_0/2}(1+e^{-\gamma_0\tilde{L}_0}R_b^p)}{1-e^{-2\gamma_0\tilde{L}_0}R_b^pR_t^p}\right]e^{-\gamma_t(\tilde{z}-\tilde{L}_{t-tot})},$$

$$\phi_b^V = \frac{p_o}{2\kappa_b}\int_{-\infty}^\infty \frac{k_0}{\gamma_b}H_0^1(\lambda\tilde{\rho})\lambda d\lambda$$

$$\times\left[\frac{T_b^pe^{-\gamma_0\tilde{L}_0/2}(1+e^{-\gamma_0\tilde{L}_0}R_t^p)}{1-e^{-2\gamma_0\tilde{L}_0}R_b^pR_t^p}\right]e^{+\gamma_b(\tilde{z}+\tilde{L}_{b-tot})} \qquad (12)$$

for the top [above the slab and top film stack (subscript t)] and bottom [below the slab and bottom film stack (subscript b)] semi-infinite outer cladding regions. In these expressions, $k_0^{-1}\tilde{L}_{t-tot}$ and $k_0^{-1}\tilde{L}_{b-tot}$ are the total physical thicknesses of the top and bottom cladding layers from the position of the dipole to the edge of the outer cladding regions as shown in Fig. 1. The Hertz potential within the film stacks is readily evaluated from these results. Here the R's and T's refer to the magnetic field reflectivity looking from inside the slab from the multilayer top (bottom) stacks for a TM wave propagating upwards (downwards) in the slab $R_t^p(R_b^p)$ and the T's are the corresponding transmissions through the entire film stacks. In the limit of a single dielectric interface at the top of the slab these reduce to the familiar results for a TM-wave incident from the slab towards the top dielectric (and similar expressions for the bottom interface)

$$R_t^p \to \frac{\kappa_t\gamma_0 - \kappa_0\gamma_t}{\kappa_t\gamma_0 + \kappa_0\gamma_t},$$

$$T_t^p = \frac{\kappa_t}{\kappa_0}(1 - R_t^p) = \frac{2\kappa_t\gamma_t}{\kappa_t\gamma_0 + \kappa_0\gamma_t}. \qquad (13)$$

Comparing this result with Eq. (10) of Ref. [1] for a simple dielectric slab, the only changes are (1) the substitution of the multilayer refection/transmission coefficients for their single interface values; (2) the separate identification of top and bottom reflection and transmission coefficients re-

quired for this generalized asymmetric calculation; and (3) setting the dipole position to the center of the slab ($a=0$ from Ref. [1]) since any shift of the dipole position can be accommodated by adding additional films (with the same dielectric constant). The bracketed terms have simple physical interpretations. There are two contributions to the fields in the top region, one direct transmission from the upward directed plane waves of the dipole and a second reflected from the bottom slab interface. The resonant denominator accounts for the multiple reflections within the slab. The zeros of this denominator correspond to poles of the integrand and, thus, the radiation into 2D bound waveguide modes. There are branch cuts in the λ plane as a result of the multivalued γ_i's. Integration around these branch cuts gives the 3D free-space radiation. The inverse transform will be discussed following the presentation of the boundary value solutions for the horizontal dipole in the next section.

B. Boundary value problem and evaluation of the Hertz potential; horizontal dipole ($\cos\theta_d=0$)

For a horizontal dipole, both ϕ and ψ must be evaluated. Since the boundary conditions are uncoupled, the solution proceeds straightforwardly using the source terms in Eq. (9) for $\theta_d=\pi/2$. The boundary conditions are [9]

$$\phi_1=\phi_2,\quad \psi_1=\psi_2,$$

$$\frac{1}{\kappa_1}\frac{\partial\phi_1}{\partial z}=\frac{1}{\kappa_2}\frac{\partial\phi_2}{\partial z},\quad \frac{\partial\psi_1}{\partial z}=\frac{\partial\psi_2}{\partial z}. \tag{14}$$

This decoupling of the boundary conditions for the two scalar functions is a major algebraic advantage of the Hertz vector representation introduced by Lukosz [9]. The solutions again are obtained by straightforward thin-film analysis based on the boundary conditions Eq. (14) and the source terms Eq. (9),

$$\psi_0^H=\frac{p_0}{2}\eta_0\int_{-\infty}^{\infty}\frac{1}{\gamma_0}\sin\varphi H_0^1(\lambda\tilde\rho)d\lambda$$

$$\times\left[\frac{e^{-\gamma_0\tilde L_0}R_b^s(1+e^{-\gamma_0\tilde L_0}R_t^s)}{1-e^{-2\gamma_0\tilde L_0}R_b^sR_t^s}e^{-\gamma_0\tilde z}\right.$$

$$\left.+\frac{e^{-\gamma_0\tilde L_0}R_t^s(1+e^{-\gamma_0\tilde L_0}R_b^s)}{1-e^{-2\gamma_0\tilde L_0}R_b^sR_t^s}e^{\gamma_0\tilde z}+e^{-\gamma_0|\tilde z|}\right],$$

$$\phi_0^H=\frac{ip_0}{2\kappa_0}\int_{-\infty}^{\infty}k_0\cos\varphi H_0^1(\lambda\tilde\rho)d\lambda$$

$$\times\left[\frac{e^{-\gamma_0\tilde L_0}R_b^p(1-e^{-\gamma_0\tilde L_0}R_t^p)}{1-e^{-2\gamma_0\tilde L_0}R_b^pR_t^p}e^{-\gamma_0\tilde z}\right.$$

$$\left.-\frac{e^{-\gamma_0\tilde L_0}R_t^p(1-e^{-\gamma_0\tilde L_0}R_b^p)}{1-e^{-2\gamma_0\tilde L_0}R_b^pR_t^p}e^{\gamma_0\tilde z}(\mp)e^{-\gamma_0|\tilde z|}\right] \tag{15}$$

for the slab, and

$$\psi_t^H=\frac{p_0}{2}\eta_0\int_{-\infty}^{\infty}\frac{1}{\gamma_t}\sin\varphi H_0^1(\lambda\tilde\rho)d\lambda$$

$$\times\frac{T_t^se^{-\gamma_0\tilde L_0/2}(1+e^{-\gamma_0\tilde L_0}R_b^s)}{1-e^{-2\gamma_0\tilde L_0}R_b^sR_t^s}e^{-\gamma_t(\tilde z-\tilde L_{t-tot})},$$

$$\phi_t^H=\frac{-ip_0}{2\kappa_t}\int_{-\infty}^{\infty}k_0\cos\varphi H_0^1(\lambda\tilde\rho)d\lambda$$

$$\times\frac{T_t^pe^{-\gamma_0\tilde L_0/2}(1-e^{-\gamma_0\tilde L_0}R_b^p)}{1-e^{-2\gamma_0\tilde L_0}R_b^pR_t^p}e^{-\gamma_t(\tilde z-\tilde L_{t-tot})}, \tag{16a}$$

$$\psi_b^H=\frac{p_0}{2}\eta_0\int_{-\infty}^{\infty}\frac{k_0}{\gamma_b}\sin\varphi H_0^1(\lambda\tilde\rho)d\lambda$$

$$\times\frac{T_b^se^{-\gamma_0\tilde L_0/2}(1+e^{-\gamma_0\tilde L_0}R_t^s)}{1-e^{-2\gamma_0\tilde L_0}R_b^sR_t^s}e^{+\gamma_b(\tilde z+\tilde L_{b-tot})},$$

$$\phi_b^H=\frac{ip_0}{2\kappa_b}\int_{-\infty}^{\infty}k_0\cos\varphi H_0^1(\lambda\tilde\rho)d\lambda$$

$$\times\frac{T_b^pe^{-\gamma_0\tilde L_0/2}(1-e^{-\gamma_0\tilde L_0}R_t^p)}{1-e^{-2\gamma_0\tilde L_0}R_b^pR_t^p}e^{+\gamma_b(\tilde z+\tilde L_{b-tot})} \tag{16b}$$

for the top and bottom semi-infinite outer cladding regions. In these expressions, $R_{t,b}^s,T_{t,b}^s$ are the electric field reflectivities for TE polarized waves incident from the slab on the respective interfaces. In the limit of a simple dielectric interface these reduce for the top interface to

$$R_t^s=\frac{\gamma_0-\gamma_t}{\gamma_0+\gamma_t},\quad T_t^s=1-R_t^s=\frac{2\gamma_t}{\gamma_0+\gamma_t}. \tag{17}$$

In Eq. (15), the minus sign in the parentheses is appropriate for $\tilde z>0$ and the plus sign for $\tilde z<0$. As mentioned above, the polar angle φ, defined relative to the orientation of the dipole in the slab, arises from the presence of the transverse transform coordinates (ξ,η) in the source terms for the horizontal dipole.

The physical interpretation of these equations is similar to that for the vertical dipole. Now the coupling is to both TE and TM radiation and bound modes. The zeros of the denominators correspond to the bound modes (TM for $1-e^{-2\gamma_0\tilde L_0}R_b^pR_t^p=0$; TE for $1-e^{-2\gamma_0\tilde L_0}R_b^sR_t^s=0$). In each numerator there is a term that corresponds to the radiation directly incident from the dipole and a second term from the radiation reflected from the opposite interface. For the potential within the slab there are upward and downward reflected

waves and the source terms. For the potential in the half-spaces the numerators correspond to transmission from the source at the center of the slab. The denominators account for the multiple reflections, and include all near field terms; no approximations to the full electromagnetic calculation have been made to this point. These approximations will be made in the branch cut integrals, which are evaluated by the method of steepest descents that is only valid far (many wavelengths) from the source point, and in the evaluation of the contributions from the poles using the asymptotic limits of the Hankel function, again valid many wavelengths from the source point. There are branch cuts corresponding to each of the thin film layers. In the half-spaces above and below the structure, only the integral around the branch cut corresponding to that specific medium contributes to the radiation fields; the other branch cuts contribute only to the near fields and thus are excluded from the subsequent analysis.

C. Evaluation of the inverse transform

The apparatus of a complex analysis can now be applied to the remaining integrals. As noted above, there are contributions due to integration around the branch cuts (corresponding to 3D radiation into the semi-infinite half-spaces above and below the structure) and due to poles of the denominators (2D bound modes). The manipulations have been presented for a single interface in great detail in Ref. [11] for a single interface and in Ref. [4] for the simple slab case. Only the final results will be presented here.

1. Vertical dipole

2D bound modes. For the vertical dipole, the Hertz potential within the slab is evaluated using the asymptotic limit of the Hankel function $[H_0^1(z) \rightarrow -i e^{iz} \sqrt{2/\pi z}]$ and taking the residues at the zeros of the denominator,

$$
\phi_0^{2D} = p_0 k_0 \sum_l \sqrt{\frac{8\pi}{k_l^p \tilde{\rho}}} e^{ik_l^p \tilde{\rho}} \frac{k_l^p}{\kappa_0 \gamma_{0,l}^p \delta D_l^p}
$$

$$
\times [(1 + R_{sym}^p e^{-\gamma_{0,l}^p \tilde{L}_0}) \cosh(\gamma_{0,l}^p \tilde{z})
$$

$$
+ R_{asym}^p e^{-\gamma_{0,l}^p \tilde{L}_0} \sinh(\gamma_{0,l}^p \tilde{z})], \quad (18)
$$

where the denominator is expanded around the roots (k_l^p, where the subscript is the mode index) of the TM (p superscript) modal dispersion relation, viz.,

$$
D_l^p = 1 - e^{-2\gamma_1 \tilde{L}_0} R_b^p R_t^p \approx (\lambda - k_l^p) \left. \frac{\partial D_p}{\partial k} \right|_{k_l^p} \equiv (\lambda - k_l^p) \delta D_l^p
$$

$$
(19)
$$

and

$$
R_{sym}^p \equiv \frac{R_t^p + R_b^p}{2}, \quad R_{asym}^p \equiv \frac{R_t^p - R_b^p}{2}. \quad (20)
$$

The superscript on the γ's takes note of the fact that they are evaluated at the roots of the TM dispersion relation and the subscripts on the γ's refer to the layer index (j) and the

mode index (l) $[\gamma_{j,l}^p \equiv \gamma_j(\lambda)|_{\lambda = k_l^p}]$. The corresponding indices on the reflection coefficients are suppressed for convenience.

From this result, the next step is to evaluate the fields and to integrate across the mode profile to get the radiated power with the result for the central slab containing the dipole,

$$
\hat{P}_{V,TM}^{2D} = \frac{3\pi k_0}{\text{Re}(\kappa_1)\sqrt{\varepsilon_0}} \sum_l \frac{|k_l^{p'}|^4}{|\delta D_l^p|^2}
$$

$$
\times \left[\begin{array}{c} [|c_{0,l}|^2 + |d_{0,l}|^2] \dfrac{\sinh(\gamma_{0,l}^{p'} \tilde{L}_0/2)}{\gamma_{0,l}^{p'}} \\[2ex] + [c_{0,l} d_{0,l}^* + c_{0,l}^* d_{0,l}] \dfrac{\sin(\gamma_{0,l}^{p''} \tilde{L}_0/2)}{\gamma_{0,l}^{p''}} \end{array} \right], \quad (21)
$$

where the summation is over all modes (l), $\gamma_{0,l}^p = \gamma_{0,l}^{p'} + i\gamma_{0,l}^{p''}$, and the coefficients $c_{0,l}$ and $d_{0,l}$ are the complex amplitudes of the upward and downward directed fields in each layer at the center of the slab. From Eq. (18)

$$
c_{0,l} = \frac{1}{2}(1 + R_{sym}^p e^{-\gamma_{0,l} \tilde{L}_0} + R_{asym}^p e^{-\gamma_{0,l} \tilde{L}_0})
$$

$$
= \frac{1}{2}(1 + R_t^p e^{-\gamma_{0,l}^p \tilde{L}_0}),
$$

$$
d_{0,l} = \frac{1}{2}(1 + R_{sym}^p e^{-\gamma_{0,l} \tilde{L}_0} - R_{asym}^p e^{-\gamma_{0,l} \tilde{L}_0})
$$

$$
= \frac{1}{2}(1 + R_b^p e^{-\gamma_{0,l}^p \tilde{L}_0}). \quad (22)
$$

Similar expressions need to be evaluated over the entire film stack, including the top and bottom semi-infinite regions, and summed to get the total 2D radiated power.

3D radiated energy. The calculation proceeds by substituting the integral expression for the Hankel function

$$
H_0^1(z) = \frac{4}{\pi} e^{iz} \int_0^\infty (4iz - y^2)^{-1/2} e^{-y^2/2} dy \approx e^{iz} \sqrt{\frac{2}{i\pi z}}, \quad (23)
$$

where the last approximation is valid in the radiation zone, many wavelengths from the dipole. Then the Hertz potential in the semi-infinite cladding regions can be evaluated by integrating around the branch cut by the method of steepest descents with the result for the top half-space:

$$
\phi_t = \frac{p_0 k_0 e^{in_t \tilde{R}}}{\tilde{R}} \frac{1 - R_t^p}{\kappa_0} \frac{[1 + e^{in_0 \tilde{L}_0 \cos(\vartheta)} R_b^p(\theta)]}{1 - e^{2in_0 \tilde{L}_0 \cos(\vartheta)} R_t^p(\theta) R_b^p(\theta)}
$$

$$
\times e^{i(n_0 \cos\vartheta - n_t \cos\theta)\tilde{L}_0/2}, \quad (24)
$$

where $\tilde{R}$ is the dimensionless radial distance coordinate, ϑ is the propagation angle inside the slab for an external angle of θ $[\cos^2 \vartheta \equiv 1 - (\kappa_t/\kappa_1)\sin^2 \theta]$ and the reflection coefficients are evaluated at the external angle θ.

For the radiated power, normalized to the power radiated by the dipole in an infinite medium, the final result is

$$\hat{P}_{TM}^{V} = \frac{3}{4} \left| \frac{\kappa_t}{\kappa_0} \right|^{5/2} \int_0^{\pi/2} \left| \frac{[1-R_t^p(\theta)][1+e^{in_0\tilde{L}_0\cos\vartheta}R_b^p(\theta)]e^{i(n_0\cos\vartheta - n_t\cos\theta)\tilde{L}_0/2}}{1-e^{2in_0\tilde{L}_0\cos\vartheta}R_t^p(\theta)R_b^p(\theta)} \right|^2 \sin^3\theta\, d\theta \tag{25}$$

with a similar expression for the power radiated into the bottom half-space with the obvious interchange ($t \Leftrightarrow b$). As expected, this result is identical to that for the simple slab [4] with the substitution of the film-stack reflectivities for those of the simple dielectric interface and the generalization to an asymmetric cladding structure.

2. Horizontal dipole

A horizontal dipole couples to both TE and TM radiation. The calculations are very similar to those presented above and only the results are given here.

2D bound modes. For TE coupling

$$\psi_0^{2D,H} = \sin\varphi\, p_0 \eta_0 \sum_l \sqrt{\frac{8\pi}{k_l^s\tilde{\rho}}} e^{ik_l^s\tilde{\rho}} \frac{1}{\delta D_l^s}$$

$$\times [(1+R_{sym}^s e^{-\gamma_{0,l}^s\tilde{L}_0})\cosh(\gamma_{0,l}^s\tilde{z})$$

$$+ R_{asym}^s {}^{-\gamma_{0,l}^s\tilde{L}_0}\sinh(\gamma_{0,l}^s\tilde{z})], \tag{26}$$

$$\hat{P}_{TE}^{2D,H} = \frac{3\pi}{4\,\mathrm{Re}(n_0)} \sum_l \left| \frac{k_l^s}{\delta D_l^s} \right|^2$$

$$\times \left[\begin{array}{c} [|c_{0,l}|^2 + |d_{0,l}|^2] \dfrac{\sinh(\gamma_{0,l}^{s\prime}\tilde{L}_0/2)}{\gamma_{0,l}^{p\prime}} \\[4mm] + [c_{0,l}d_{0,l}^* + c_{0,l}^* d_{0,l}] \dfrac{\sin(\gamma_{0,l}^{s\prime\prime}\tilde{L}_0/2)}{\gamma_{0,l}^{p\prime\prime}} \end{array} \right],$$

$$c_{0,l} = \frac{1}{2}(1+R_t^s e^{-\gamma_{0,j}^s\tilde{L}_0}),$$

$$d_{0,j} = \frac{1}{2}(1+R_b^s e^{-\gamma_{0,j}^s\tilde{L}_0}). \tag{27}$$

For TM coupling

$$\phi_0^{2D,H} = \cos\varphi\, p_0 k_0 \sum_l \sqrt{\frac{8\pi}{k_l^p\tilde{\rho}}} e^{ik_l^p\tilde{\rho}} \frac{1}{\delta D_l^p}$$

$$\times [(1-R_{sym}^p e^{-\gamma_{0,l}^p\tilde{L}_0})\sinh(\gamma_{0,l}^p\tilde{z})$$

$$- R_{asym}^p e^{-\gamma_{0,l}^p\tilde{L}_0}\cosh(\gamma_{0,l}^p\tilde{z})] \tag{28}$$

$$\hat{P}_{TM}^{2D,H} = \frac{3\pi}{4\,\mathrm{Re}(\kappa_0^{3/2})} \sum_l \left| \frac{k_l^p}{\delta D_l^s} \right|^2$$

$$\times \left[\begin{array}{c} [|c_{0,l}|^2 + |d_{0,l}|^2] \dfrac{\sinh(\gamma_{0,l}^{p\prime}\tilde{L}_0/2)}{\gamma_{0,l}^{p\prime}} \\[4mm] + [c_{0,l}d_{j,l}^* + c_{0,l}^* d_{j,l}] \dfrac{\sin(\gamma_{0,l}^{p\prime\prime}\tilde{L}_0/2)}{\gamma_{0,l}^{p\prime\prime}} \end{array} \right],$$

$$c_{0,j} = \frac{1}{2}(1-R_t^p e^{-\gamma_{0,j}^p\tilde{L}_0}),$$

$$d_{0,j} = -\frac{1}{2}(1-R_b^p e^{-\gamma_{0,j}^p\tilde{L}_0}). \tag{29}$$

3D radiation into top half-space. For TE coupling

$$\psi_t^H = p_0 k_0 \eta_0 \frac{\sin\varphi}{\sin\theta} \left(\frac{e^{ik_t\tilde{R}}}{n_t\tilde{R}} \right) T_t^s \frac{1+R_b^s e^{in_0\tilde{L}_0\cos\vartheta}}{1-R_t^s R_b^s e^{2in_0\tilde{L}_0\cos\vartheta}}$$

$$\times e^{i(n_0\cos\vartheta - n_t\cos\theta)\tilde{L}_0/2}, \tag{30}$$

$$\hat{P}_{TE,t}^{3D,H} = \frac{3}{8}\mathrm{Re}\left(\frac{n_t}{n_0} \right) \int_0^{\pi/2}$$

$$\times \left| T_t^s \frac{1+R_b^s e^{in_0\tilde{L}_0\cos\vartheta}}{1-R_t^s R_b^s e^{2in_0\tilde{L}_0\cos\vartheta}} e^{i(n_0\cos\vartheta - n_t\cos\theta)\tilde{L}_0/2} \right|^2$$

$$\times \sin(\theta)\,d\theta. \tag{31}$$

For TM coupling

$$\phi_t^H = p_0 k_0 \frac{\cos\theta\cos\varphi}{\sin\theta} \left(\frac{e^{in_t\tilde{R}}}{n_t\tilde{R}} \right) T_t^p \frac{-1+R_b^p e^{in_0\tilde{L}_0\cos\vartheta}}{1-R_t^p R_b^p e^{2in_0\tilde{L}_0\cos\vartheta}}$$

$$\times e^{i(n_0\cos\vartheta - n_t\cos\theta)\tilde{L}_0/2}, \tag{32}$$

$$\hat{P}_{TM,t}^{3D,H} = \frac{3}{8}\mathrm{Re}\left(\frac{n_t}{n_0} \right) \int_0^{\pi/2}$$

$$\times \left| n_t T_t^p \frac{-1+R_b^p e^{in_0\tilde{L}_0\cos\vartheta}}{1-R_t^p R_b^p e^{2in_0\tilde{L}_0\cos\vartheta}} e^{i(n_0\cos\vartheta - n_t\cos\theta)\tilde{L}_0/2} \right|^2$$

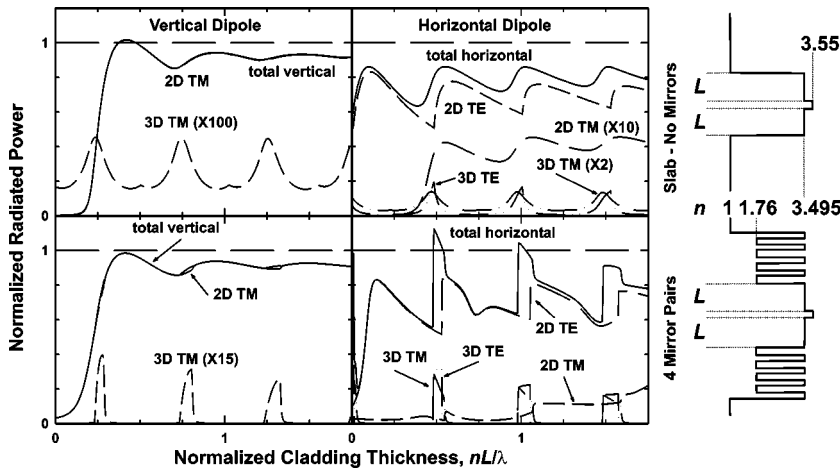$$\times \cos^2(\theta)\sin(\theta)\,d\theta. \tag{33}$$

FIG. 2. Radiated power from a dipole embedded in a slab (top) and in the same slab with four mirror stacks (bottom). The results for a vertical dipole are shown in the left panels and for a horizontal dipole in the right panels. In each case the dipole is embedded in a thin (10-nm-wide) InGaAs ($n=3.55$) section clad top and bottom with GaAs ($n=3.495$) spacers of thickness L. For the slab, the semi-infinite outer claddings are air ($n=1$); for the mirror stacks are $\lambda/4$ pairs of Al$_2$O$_3$ ($n=1.76$) and GaAs, again with semi-infinite air outer claddings. See text for detailed discussion.

with equivalent expressions for the radiation into the bottom half space.

Again, it is instructive to compare these expressions for a horizontal dipole with the equivalent expressions derived for the symmetrically clad slab with Sommerfeld's Hertz vector approach [4]. For the TE coupling the results are again very similar with the straightforward substitutions of the multilayer reflectivities, the more careful tracking of reflection coefficients necessary for nonequivalent surfaces, and the automatic placement of the dipole in the center of the slab. The TM results are significantly simpler in this formulation, particularly for the Hertz potential and the 3D radiation contributions. In the previous treatment, based on the Sommerfeld formulation, the possible algebraic simplification was only recognized for the bound mode contributions.

IV. RESULTS

In the following two sections, results using these expressions are presented for two related vertical-cavity structures. First, we consider a slab bound by two symmetric quarter wavelength mirror stacks with air on both sides. The power is radiated into both bound modes and 3D radiation. In the second case, the same structures are atop a GaAs substrate, again with air cladding the top surface. Now there are no bound modes, but there are "leaky" modes with field distributions very similar to the bound modes, but whose energy leaks into radiation modes in the substrate. Absorption has been set to zero (all indices taken as pure real quantities), interface roughness has been neglected, and the structure is taken as infinite within the plane. Additionally, the dipole radiation has been assumed to be at a continuous single frequency ω, without any dephasing (T_2) or decay (T_1) events. The impact of all of these assumptions is to allow the coherent addition of fields over many transits of the multilayer structure, e.g., to investigate very high finesse resonances. This allows beautiful examples of resonance effects; however, due consideration of these limiting effects must be taken in applying this analysis to the interpretation of experimental results.

A. Slab with DBR mirrors—bound modes and radiation

The slab structure consists of a thin (10 nm) InGaAs quantum well ($n=3.55$) with the dipole in the center of the

well, symmetric GaAs inner cladding layers ($n=3.495$) whose thicknesses are equal and are varied in the calculation, symmetric $\lambda/4$ Al$_2$O$_3$/GaAs ($n=1.76/3.495$) mirror pairs (results for zero to four mirror pairs are presented), and air ($n=1$) upper and lower outer cladding half-spaces. The spatial index profile is shown as an inset in Fig. 2. These index values are appropriate to a wavelength of 980 nm; results are shown normalized to the wavelength in the GaAs layers.

The calculated radiated power, normalized to the radiated power in an unbounded InGaAs medium as a function of the GaAs inner cladding thickness for a simple slab (top, no mirror stacks) and for a slab bound on each side by four mirror stacks (bottom) is shown in Fig. 2 for both a vertical dipole source (left) and a horizontal dipole source (right). For the vertical dipole source, all of the radiation is into TM bound and radiation modes. For the air-clad slab, the 3D radiation shows strong Fabry-Perót resonances for slab thicknesses near $2n_1\tilde{L}\sim(2j+1)\lambda/2$, $j=0,1,\ldots$, and much weaker resonances for even numbers of half-wave resonances. This alternation arises from the factoring of the resonant denominator for this symmetric case and the cancellation of one set of resonances by the numerator in Eq. (25). The horizontal dipole has a similar set of resonances but now at even numbers of half-waves and the cancellation for odd numbers of half-waves, for both the TE and TM radiation components. These resonance conditions are a direct consequence of the boundary conditions in Eqs. (10) and (14). The TM radiation boundary conditions for a vertical dipole require that the Hertz potential be zero at the edges of the inner cladding as the magnitude of the reflectivity approaches unity, whereas the TE and TM boundary conditions for a horizontal dipole force the derivative of the potential to zero at the same locations. The high symmetry of a dipole located in the precise center of the slab results in these alternating resonance selection rules; more complex behavior is found for a dipole displaced from the center of the slab. For the 2D bound modes, the vertical dipole exhibits a strong suppression of the radiation for very thin slabs ($L\ll\lambda/n$) while the radiation is more pronounced for the horizontal dipole at these thicknesses. In both cases, the total radiated power rises approximately to that for the dipole in an infinite medium as the inner cladding thickness is increased; the slightly lower value (<1) than in an infinite InGaAs medium is be-

cause the normalization is to the dipole in the higher index InGaAs, but the majority of the bound mode radiation is confined to the GaAs layers. Each of the contributions to the total radiated power has been multiplied by various factors to make them visible in the figure. As is well known, for the vertical dipole, only very weak radiation into the air spaces is observed (3D×100). More interesting is the result for the horizontal dipole, where most of the radiation is into the TE mode; the 2D TM radiation is multiplied by 10, while the 3D TM radiation contribution to the total power is multiplied by 2.

The impact of the mirror pairs on the distribution of power between the individual radiation components is significant, whereas the total radiated power is only modestly impacted. For a vertical dipole, there is a noticeable increase in the radiated power into the 2D TM mode for very thin slabs. This is a result of the increased mode volume due to the mirrors (see the left side of Fig. 2). For the air-clad slab, only the lowest-order mode is propagating for $2n_1 L \lesssim \lambda$ while for the four-mirror-clad slabs, there are six propagating modes even for $\tilde{L}=0$. For both dipole orientations, the 3D radiation is significantly increased at the alternating half-wave resonances, and suppressed away from these resonances. For a horizontal dipole at the first two resonances, the total radiated power is slightly larger (~15%) than that for a dipole in an infinite medium corresponding to a decrease in the radiative lifetime. The 3D radiation is strongly peaked at the even integral resonances for both the TE and TM components. Away from these resonances, essentially all of the radiated power is in the 2D bound modes. As the number of mirror pairs is increased, more of the energy is shifted into the TM radiation, although it remains a significantly smaller fraction of the total power than that radiated into the TE mode. There is a more equal balance of radiated power between TE and TM for the 3D radiation.

The evolution of the total radiated power as the number of mirror pairs is shown more clearly in Fig. 3. Results are shown for both vertical (top) and horizontal (bottom) dipoles for the slab case and for one through four mirror pairs. The curves are offset for clarity. In each case, the radiation from a dipole in an infinite medium is shown as the associated dotted line.

For a vertical-cavity laser, the radiated power for a horizontal dipole in the normal direction, perpendicular to the layers, is of particular interest. The maximum intensity into the normal direction occurs when the TE and TM powers are equal, just at the leading edge of the resonances of Fig. 2 (see also Fig. 5B). Figure 4 (top) shows the normalized forward direction emission for a horizontal dipole as a function of the slab thickness for the five cases of a slab and one through four mirror pairs. The angular variation at the peak is also shown in Fig. 4 (bottom). The variation with slab thickness shows the expected Lorentzian line shape from the expansion of the resonant denominator at an increasing cavity finesse F as the reflectivity increases with the number of mirror pairs. (The calculated normal emission power reflectivities and corresponding F's are $|R|^2 = 0.31$, $F \sim 2.5$, slab; $|R|^2 = 0.75$, $F \sim 11$, one mirror pair; $|R|^2 = 0.93$, $F \sim 43$, two mirror pairs; $|R|^2 = 0.982$, $F \sim 173$, three mirror
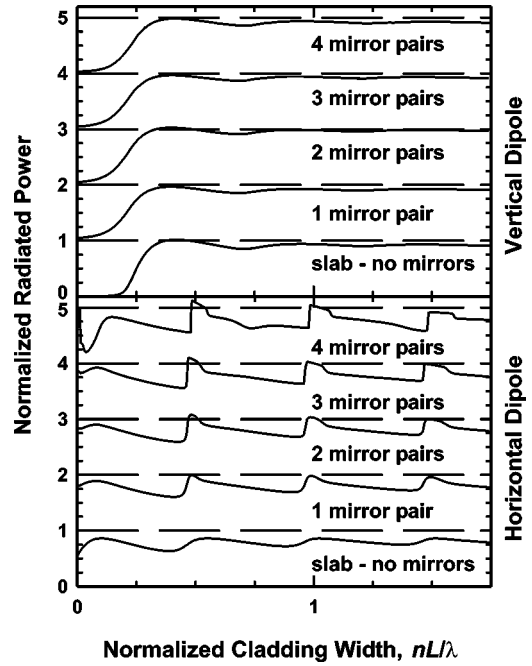

FIG. 3. Evolution of the total radiated power for a symmetric structure as the number of mirror pairs is varied. The curves are offset for clarity; in each case the dashed line represents the power radiated by the dipole into an infinite InGaAs medium.

pairs; and $|R|^2 = 0.995$, $F = 628$, four mirror pairs.) The slight shift of the resonance away from $2nL/\lambda = 1$ is due to the optical thickness of the InGaAs quantum well. As ex-
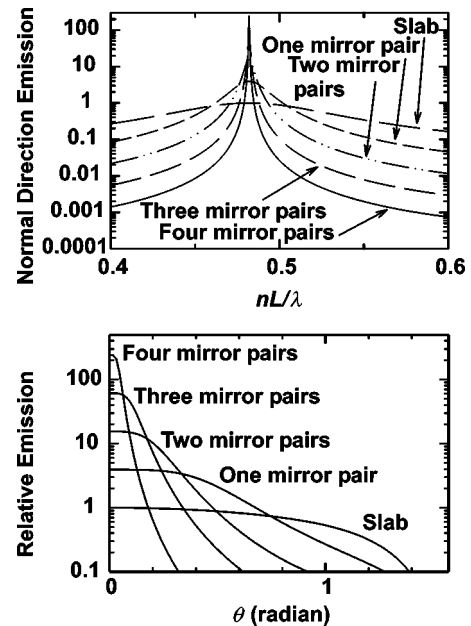

FIG. 4. Vertical emission (normal to the layer structure) into 3D radiation modes for a horizontal dipole embedded in a symmetrically clad slab as a function of the inner cladding thickness (top) and the angular variation for the peak vertical emission (bottom), both with the number of mirror pairs as a parameter. As expected, the increasing finesse of the resonance with increasing numbers of mirror pairs is reflected in both plots.
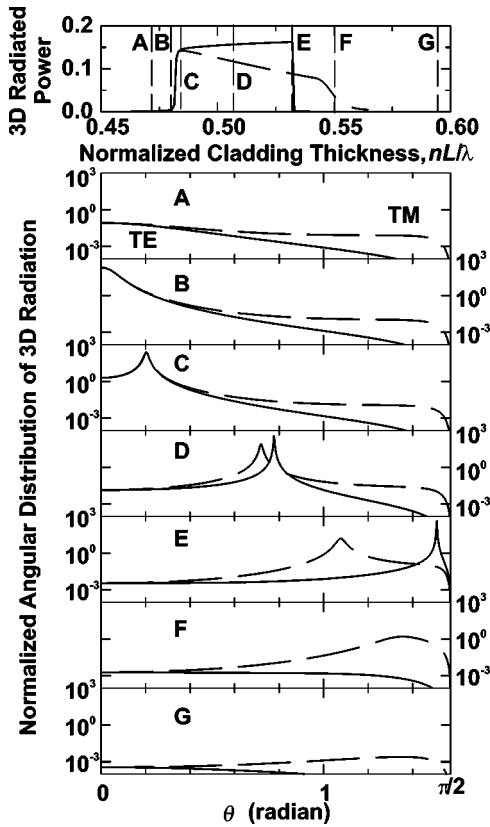
FIG. 5. Angular variation of the 3D radiation from a horizontal dipole in a symmetrically clad slab with four mirror pairs as the inner cladding thickness is varied. The top panel shows an expanded view of the integrated TE and TM 3D radiation in the vicinity of the first-resonance inner cladding thickness. The angular traces (A though G) show the evolution of the angular dependence of the emission as the inner cladding thickness is varied in this region.

pected, the angular variation of the emission at the peak of each of these resonances narrows significantly as F increases.

As the inner cladding thickness L increases beyond this resonance, the peak of the 3D emission shifts to steeper angles for both TE and TM radiation, and the total 3D radiated power increases dramatically. The top panel of Fig. 5 shows an expanded view of the total integrated 3D radiated power emitted from both surfaces around the first peak region ($nL/\lambda \sim 0.5$) for the four-mirror-pair case for a horizontal dipole. From the symmetry of this geometry, the same power is emitted from both surfaces. The angular dependence of the radiated power is shown for various values of L (A through G) as indicated in the top panel. Case A is before the resonance; the radiated power is quite small and does not show a pronounced angular dependence. Case B is the maximum of the normal-direction emitted power shown previously in Fig. 4. Notice that this peak normal emission corresponds to a very small fraction of the power radiated from the dipole. Case C is just past the sharp increase in the 3D emitted power for both TE and TM radiation. There is a peak in the angular dependence, for both TE and TM radiation, at a small angle away from normal. This peak can be traced to

the round-trip resonance condition in the denominators [Eqs. (31) and (33)] that must move away from normal as the thickness is increased. The explicit dependence in Eqs. (31) and (33) is on the thickness of the central slab medium containing the dipole, which is fixed in this calculation. The dependence on the thickness of the cladding is contained in the phase of the reflection coefficients. This lowest order round trip resonance condition is simply, $4n_{GaAs}\cos\vartheta_{GaAs}L + 2n_{InGaAs}\cos\vartheta L_{InGaAs} + 2\phi(\theta) = \lambda/2\pi$, which clearly exhibits the dependence of ϑ_{GaAs}, the angle of propagation in the inner cladding, on L. The final phase term $\phi(\theta)$ represents the phase shift in the reflector stack beyond the inner cladding. The external angle θ is related to ϑ_{GaAs} by the Fresnel condition $n_{GaAs}\sin\vartheta_{GaAs} = \sin\theta$ for the present case of a semi-infinite air ($n_t = 1$) outer cladding. The change in the external angle for a given change in L is amplified by the GaAs refractive index. For case D, corresponding roughly to the middle of the thickness region with substantial radiation, the peaks for TE and TM radiation occur at different angles and the TE peak is significantly sharper. This is because of the lower TM reflectivity related to Brewster's angle for TM radiation incident on a single interface. The splitting is due to phase shifts as the angle is increased. This trend is continued for case E, just before the cutoff of the TE radiation. The angular peak in the TE emission is close to $\pi/2$. For a further increase in the inner cladding thickness, the peak shifts beyond the angle for total internal reflection and the emitted power shifts from 3D radiation out the sides of the structure to 2D modes propagating within the structure. This same transition is more gradual for the TM radiation (case F) consistent with the more gradual onset of the 2D TM emission with inner cladding thickness seen in Fig. 2. Finally, case G is for a thickness beyond the significant 3D emission region where the total 3D power is weak and again does not show any strong angular dependence.

B. Active region and mirrors on substrate—No bound modes

We now make a change in the structure, replacing the bottom semi-infinite air cladding with a semi-infinite GaAs cladding. This simple change greatly modifies the calculation, but of course the results should not be dramatically different since, at least as the number of mirrors is increased, the dipole should not "see" the substrate refractive index. The major change in the calculation is that there are no bound modes in this structure, in the sense that the zeros of the dispersion relation all correspond to "modal" indices that are lower than the GaAs substrate refractive index for the entire thickness region L investigated. Thus the radiated power is either emitted out the top surface, or "leaks" from the film stack into the GaAs substrate. As before, some of the power is radiated into the upper air space. Mathematically, having the substrate index higher than the solution to the dispersion relation puts the poles on a different sheet of the Riemann surface of the inverse transform integrand (e.g., the negative sign must be taken for the square root corresponding to the substrate propagation constant whereas a positive sign was taken in the true bond mode case) so that the poles do not contribute to the inverse transform integration.
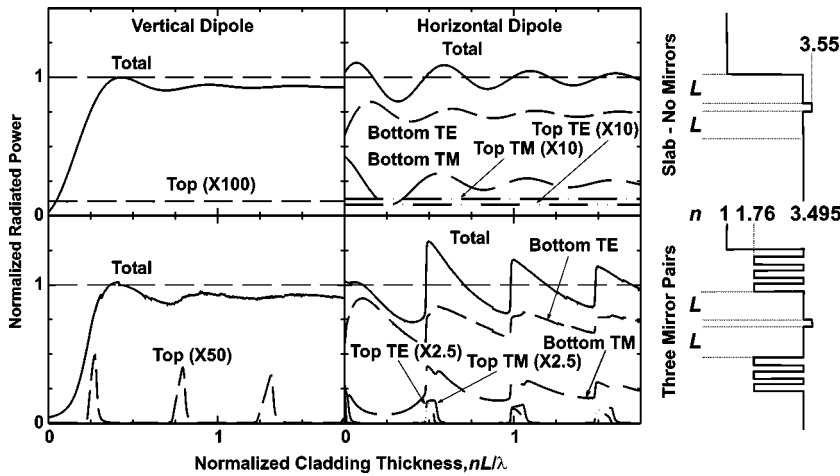
FIG. 6. Radiated power from a dipole embedded in an asymmetric film structure with air upper and GaAs lower outer claddings. The top panels are for a simple InGaAs/GaAs structure, the bottom panels include three $Al_2O_3/GaAs$ $\lambda/4$ mirror pairs. In each case the dipole is embedded at the center of a thin InGaAs region. The left panels are for a vertically oriented dipole; the right for a horizontal dipole. The only emission is into 3D radiation for these cases. There are no strictly bound modes, however, for the three mirror-pair case; there are "leaky" modes largely confined to the film stack but with radiation that leaks into the substrate.

Figure 6 shows the total radiated power for a simple slab case (top), with just a buried InGaAs layer, and for three mirror pairs (bottom). Results are shown for both a vertical dipole (left) and a horizontal dipole (right). As there are no bound modes, there are no 2D contributions; the calculation proceeds only from Eqs. (31) and (33) and their bottom surface counterparts. For a vertical dipole, the results are very similar to those for the symmetrically clad slab with air on both sides. There are somewhat larger differences for a horizontal dipole. The roughly factor of two decrease compared with the equivalent figure for the symmetrically clad geometry is due to the counting of the radiated power out of both top and bottom surfaces in Figs. 2 and 5, whereas the top and bottom surface radiated powers are shown individually in this figure. There are differences in the details of the emission dependence on inner cladding thickness that will be discussed in conjunction with Figs. 8 and 9. The total horizontal dipole emission does not exhibit the sharp transitions between 2D and 3D emission that characterized the symmetric air-clad slab, but the overall dependence of the emission on the inner cladding thickness is similar. The total emission at the peak around $nL/\lambda \sim 0.5$ is larger than for the similar symmetric air-clad three-mirror-pair case. There is also a significant change in the distribution of energy between TE and TM emission, the TM emission being more pronounced in this substrate geometry.

Figure 7 shows the progression of the total emitted power as a function of the inner cladding thickness with the number of mirror pairs as a parameter. The curves have been offset for clarity. The radiated power for a dipole in an infinite medium is shown as the dashed line associated with each curve.

An expanded view of the first top surface emission region for a horizontal dipole, in the vicinity of $nL/\lambda \sim 0.5$, is shown in the top panel of Fig. 8. This should be compared with the comparable panel in Fig. 5 for the symmetrically air-clad slab. Again, the overall results are similar, but there are some noticeable differences. The overall shapes are inverted, in Fig. 5 the TE power increases slightly as the inner cladding thickness increases up to a very sharp cutoff while the TM power decreases and shows a much more gradual cutoff. In Fig. 8 the TM power increases while the TE power decreases as the inner cladding thickness increases. The lim-

its of the emission with inner cladding thickness are more gradual and less well defined for this case. The TM emission is larger than the TE, the opposite of the symmetrically clad slab case.

The angular dependencies of the emission out the top (air-clad) surface are shown in panels A through G. Panel A is for inner cladding thicknesses smaller than those that correspond to the peak emission. The emission is relatively weak and featureless. Panel B corresponds to the peak of the normal emission. Notice that this peak occurs for a thickness further up the knee of the emission than was the case for the symmetrically air-clad slab (Fig. 5B). Nonetheless, the emission is weaker in the present asymmetric case. In comparable units, the emission at normal for the air-clad case with three mirror pairs was 60, both top and bottom; in this case it is 11
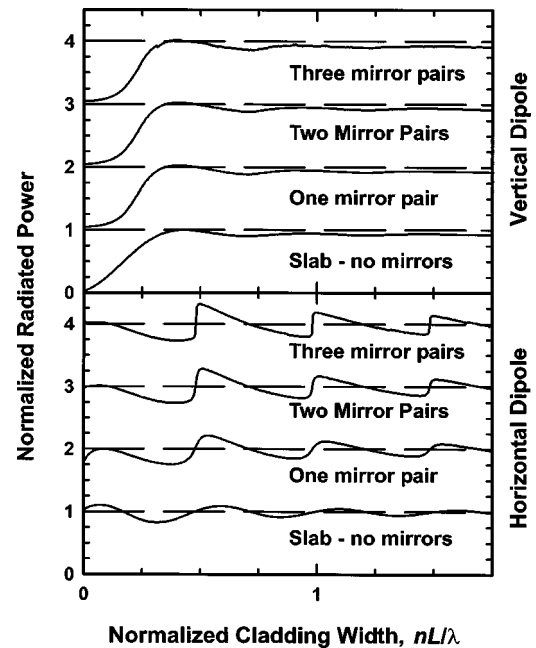

FIG. 7. Evolution of the total radiated power for an asymmetrically clad slab with an air upper and a GaAs substrate lower cladding. The curves have been offset for clarity; in each case the dashed line represents the power radiated by the dipole into an infinite InGaAs medium.
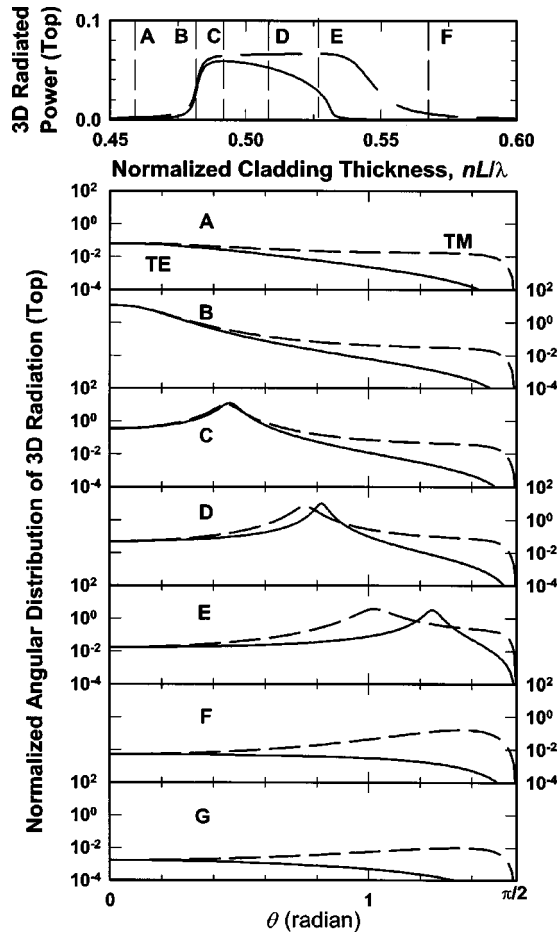
FIG. 8. Angular variation of the 3D radiation (horizontal dipole) from the top (air) surface of an asymmetrically clad slab (air upper and GaAs lower outer claddings) with three mirror pairs as the inner cladding thickness is varied. The top panel shows an expanded view of the integrated TE and TM 3D radiation in the vicinity of the first-resonance inner cladding thickness. The angular traces (A though G) show the evolution of the angular dependence of the emission as the inner cladding thickness is varied in this region. Curve G is for a normalized inner cladding thickness $nL/\lambda \sim 0.65$, beyond the thicknesses plotted in the top curve.

top and 134 bottom. Overall the normal emission is comparable, but much is lost to substrate emission in this asymmetric case. Panel C is for an inner cladding thickness near the peak TE emission. Both TE and TM emissions show comparable peak emission angles as was the case for Fig. 5. Panel D is for an inner cladding thickness near the mid point of the significant top-surface emission. As was the case for the symmetrically clad structure, at these higher angles a splitting is observed between the TE and TM peak emission angles as a result of different phase contributions from the TE and TM reflectivities. Panel E is for a thickness near the upper edge of the TE emission. The peak of the TE emission is close to $\pi/2$ as expected. Panels F and G are at the upper edge of the TM emission and beyond both TE and TM emission regions. Panel G is for a nL/λ of 0.65, outside the range of the top panel, which was plotted on the same horizontal scale as Fig. 5 for comparison. Since these curves are for emission out the top surface, the same amplification of the

external angle relative to the internal angle as was found for the previous symmetrically clad structure is also found in these cases.

In contrast to the relatively orderly behavior of the top surface emission shown in Fig. 8, the bottom surface emission shows a much more pronounced angular dependence as shown in Fig. 9 for five different values of the normalized inner cladding thickness, again for a horizontal dipole. Note the much larger vertical axis scale from 10^{10} to 10^{-5}. The TE and TM emission angular dependencies are shown side by side for clarity in this figure. The top pair of panels is for the same inner cladding thickness as panel B of Fig. 8, just at the peak of the normal emission. In addition to the angular peak at $\phi = 0$, both the TE (left) and TM (right) emission show additional structure. There are sharp dips, which are relatively independent of inner cladding thickness and are related to changes in reflectivity. A notable feature is the very strong peak in the TE emission at $\phi \sim 1.25$ (labeled TE1) and the comparable, but significantly smaller peak in the TM emission at $\phi \sim 0.66$ (TM1). These correspond to energy transmitted into the substrate from the lowest order "leaky" mode. That is from a field distribution in the upper cladding layers that looks very similar to the zero-order bound mode for the symmetrically air-clad structure. Compared to the peak normal emission of ~ 134 into the substrate, the value of this emission is 5×10^7! The resonance linewidth is correspondingly narrow, so the normalized integrated radiated power is ~ 0.5 as shown in Fig. 6. As the inner cladding thickness is increased, both TE1 and TM1 peaks shift to steeper angles. Since the refractive index of the substrate (3.495) is very similar to that of the InGaAs slab (3.55), the amplification of the angle by refraction is small. As the inner cladding thickness is further increased, both of these peaks saturate at angles close to $\pi/2$. The last pair of panels in Fig. 9 is for an inner cladding thickness such that there are two propagating leaky modes and consequently two pairs of sharp peaks, TE1 and TE2 and TM1 and TM2. These very sharp angular dependences posed some numerical integration challenges. It was easy to miss the peak in the overall integrals [the bottom surface equivalents of Eqs. (31) and (33)]. Care had to be taken to track the peaks as a function of inner cladding thickness and integrate carefully over the peak with a very fine step size to get accurate results. This is also the reason that only the three-mirror-pair rather than the four-mirror-pair case was evaluated for the asymmetric structure; the resonances became too narrow and too peaked to deal with within the 16-bit precision of the present computer program. Adding losses to the dielectric constant limits the peak value, but also results in energy loss to absorption within the dielectric stack that must be accounted for in evaluating the total radiated energy.

V. SUMMARY AND CONCLUSIONS

A fully analytic treatment of the radiation from a dipole embedded in an arbitrary dielectric stack has been presented. The treatment starts from a Hertz-vector formalism introduced by Sommerfeld [1] and extended by Lucosz [9]. The analysis proceeds by finding the Fourier transform of the
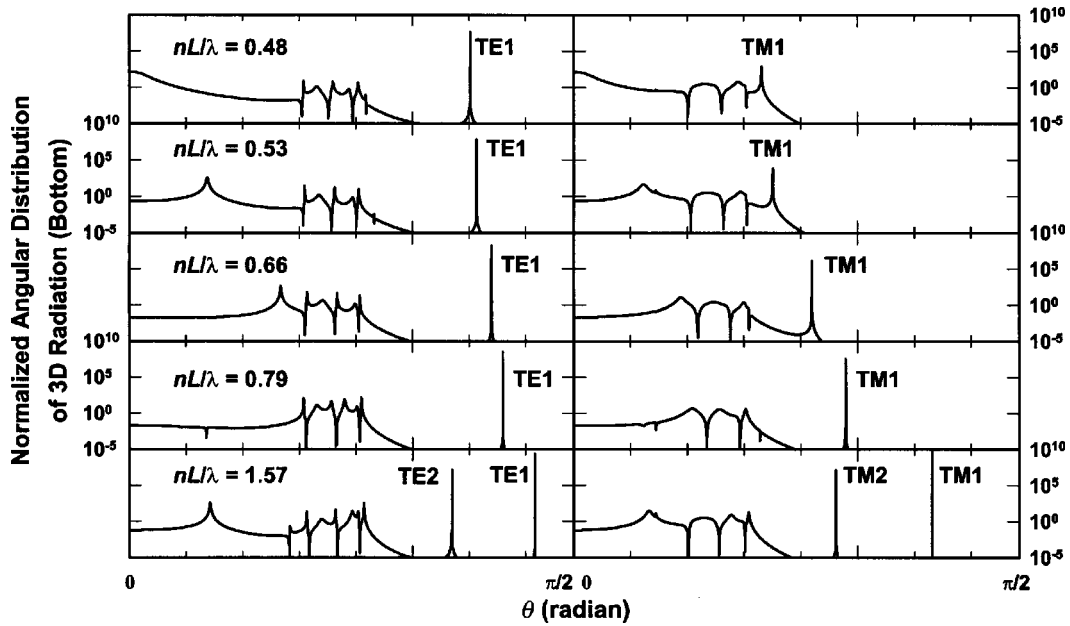
FIG. 9. Angular variation of the 3D radiation from the bottom (GaAs substrate) of an asymmetrically clad slab (air upper and GaAs lower) with three mirror pairs as the inner cladding thickness is varied for a horizontal dipole. The various values of nL/λ are given in the figure. The top panels, $nL/\lambda = 0.48$, correspond to position B, the peak normal emission, in Fig. 8 (top). The second set of panels, $nL/\lambda = 0.53$, corresponds to position E, the edge of the TE emission peak, in Fig. 8 (top). The third row of panels, $nL/\lambda = 0.79$, corresponds to a cladding thickness just before the emergence of the second top-surface emission peak (Fig. 6). The final row of panels, $nL/\lambda = 1.57$, corresponds roughly to the middle of the third top-surface emission peak in Fig. 6.

dipole fields for an unbounded medium, solving the independent boundary conditions across the multilayer stack for each Fourier component, and transforming back to real space. This procedure provides a rigorous solution to the multilayer boundary conditions. Two different classes of singularities are present in the integrand for the inverse transform: poles that correspond to bound 2D waveguide modes confined within the multilayer stack, and branch cuts that correspond to 3D radiation emitted from the sides of the stack into the upper and lower outer cladding half-spaces. While the boundary conditions are strictly valid, approximations are made in order to evaluate the radiated fields that are accurate only many wavelengths from the position of the dipole, e.g., in the radiation zone away from the near fields. The results are directly related to previous work [4] that investigated a simple dielectric slab geometry with the straightforward replacement of single layer reflectivities with their multilayer counterparts.

This formalism was applied to two closely related structures, both of which are germane to the design of semiconductor vertical-cavity lasers. Both structures contain a thin active region containing the dipole with symmetric inner claddings and an equal numbers of Bragg reflector mirror pairs on both sides. In the first case, the structure is fully symmetric with an air cladding both above and below the stack. In the second case, the lower cladding is replaced with a substrate with the same refractive index as the inner cladding. These two cases illustrate some interesting points. For the symmetrically air-clad structure, the dipole couples to both the bound modes of the slab and the radiation fields in the air spaces. For the asymmetric structure, on the other

hand, there are no bound modes because of the high-index outer cladding and only the 3D radiation calculation is operative. However, for high reflectivities, e.g., a sufficient number of Bragg reflector pairs, the results should be essentially equivalent since the dipole can not "see" the substrate because of the high reflectivity. Instead of true bound modes, there are leaky modes that look very much like the bound modes of the air-clad structure, but whose power is transmitted into the substrate after many round trips within the film stack. Because of the very high reflectivities in these structures, especially at steep angles, very sharp angular dependences are found for this radiated power, corresponding to the bound modes in the symmetric air-clad case. In both cases, the 3D radiation into the upper low-index (air) half-space is a sharp function of the thickness of the inner cladding with TM and TE resonances at alternating half-wave inner cladding thicknesses. The asymmetric case is very close to that of some LEDs on solid substrates. For example, visible-emission, nitride-based quantum-well LEDs [13] are examples of mode-free structures [14]. Modes similar to guided modes but losing power due to leakage into the substrate are observed in such structures.

Finally, we present the following conclusions.

(1) Analytic solutions are presented using a rigorous Hertz-vector formalism for dipole emission within a multilayer dielectric structure. These solutions are suitable for application to edge-emitting and vertical-cavity surface-emitting lasers (VCSELs), resonant light-emitting diodes and photodetectors, and other multilayer optoelectronic devices. Expressions are presented as functions of a normalized optical thicknesses of the various layers and can be used to ana-

lyze either thickness or wavelength variations.

(2) Enhancement/suppression of the dipole radiation relative to that in an infinite medium is obtained. The results are very dependent on the structure; however, even with a very high finesse planar cavity, the maximum enhancement is limited to $\sim 31\%$ for a horizontal dipole at the first resonance peak, e.g., for a total inner cladding thickness of $\sim n\lambda$. The inner cladding thickness for peak emission is close to, but slightly longer than, the peak normal emission thickness.

(3) A larger fractional suppression of the dipole emission is found for a vertical dipole for very short inner-cladding thicknesses lengths $\ll n\lambda/2$. This is due to destructive interference between the radiated and reflected fields at the position of the dipole.

(4) The distribution of the radiated power between 3D radiation into the outer claddings and 2D radiation into the waveguide modes shows a larger variation with structure than does the total radiated power. For a free-standing symmetric structure, the addition of high-reflectivity Bragg mirrors modifies significantly the fraction of power emitted into the air space and its inner cladding thickness and angular variations. As expected, the angular width and inner cladding thickness tolerance of the normal-emission resonance decreases with increasing mirror reflectivities.

(5) In the asymmetric case, with a high-index substrate, the bound modes of the structure evolve into leaky modes whose energy is radiated into the substrate. The top-surface emission for this case is similar to that for the symmetric case. The bottom (substrate) 3D emission is characterized by a complex dependence at small angles corresponding to the reflectivity coefficient for this multilayer structure, and by very intense and narrow resonance peaks at higher angles corresponding to the leaky modes.

---

[1] A. Sommerfeld, Ann. Phys. (Leipzig) **28**, 665 (1909).

[2] A. Sommerfeld, *Partial Differential Equations in Physics* (Academic Press, New York, 1949).

[3] D. Marcuse, *Theory of Dielectric Optical Waveguides* (Academic Press, San Diego, 1991).

[4] S. R. J. Brueck, IEEE J. Sel. Top. Quantum Electron. **JSTQE-6**, 899 (2000).

[5] G. Björk, S. Machida, Y. Yamamoto, and K. Igeta, Phys. Rev. A **44**, 669 (1991).

[6] H. Rigneault and S. Monneret, Phys. Rev. A **54**, 2356 (1996).

[7] Y. Xu, R. K. Lee, and A. Yariv, Phys. Rev. A **61**, 033807 (2000).

[8] S.-T. Ho, Y. Chu, J.-P. Zhang, S. Wu, and M.-K. Chin, in *Optical Processes in Microcavities*, edited by R. K. Chang and A. J. Campillo (World Scientific, Singapore, 1996), pp. 339–387.

[9] W. Lukosz and R. E. Kunz, J. Opt. Soc. Am. **67**, 1607 (1977).

[10] W. Lukosz, Phys. Rev. B **22**, 3030 (1980).

[11] A. Baños, *Dipole Radiation in the Presence of a Conducting Half-Space* (Pergamon Press, Oxford, 1966).

[12] J. A. Stratton, *Electromagnetic Theory*, 1st ed. (McGraw-Hill, New York, 1941), pp. 573–575.

[13] S. Nakamura, M. Senoh, N. Iwasa, and S. Nagahame, Jpn. J. Appl. Phys., Part 2 **34**, L797 (1995).

[14] I. V. Akimova, P. G. Eliseev, M. A. Osinski, and P. Perlin, Quantum Electron. **26**, 1039 (1996).